

TOWARDS INDIRECT IN VIVO MEASUREMENT OF MATERIAL PROPERTIES OF AORTIC ANEURYSMS: DETERMINING THE DISPLACEMENT FIELD

RÓBERT NAGY¹, CSABA CSOBAY-NOVÁK², ATTILA LOVAS³, PÉTER SÓTONYI⁴ AND IMRE BOJTÁR¹

¹ Department of Structural Mechanics, Faculty of Civil Engineering, Budapest University of Technology and Economics, Budapest, Hungary, robert.nagy@mail.bme.hu

² Heart Center, Faculty of Medicine, Semmelweis University, Budapest, Hungary

³ Department of Geometry, Faculty of Natural Sciences, Budapest University of Technology and Economics, Hungary

⁴ Department of Vascular Surgery, Faculty of Medicine, Semmelweis University, Budapest, Hungary

Keywords: *abdominal aortic aneurysm, risk of rupture, in vivo measurement, material parameters, ECG-gated CTA, clinical application*

Abstract: We introduce the first out of three stages of a project aiming at developing a decision procedure on abdominal aneurysm treatment in clinical practice. Going beyond the statistically backed up diameter and growth rate based routine and the state-of-the-art stress based fluid-structure interaction modelling; we develop a faster, patient specific method based on the degree of degradation determined by indirect local identification of material properties. As the first milestone, having captured the aneurysm wall position in time using in-vivo ECG-gated CTA imaging, after a smoothing algorithm compensating for the measurement errors, we are able to approximate the displacement of each material point through a complete cardiac cycle based on numerical modelling observations. The resulting strain and strain rate field provide the foundation of the final optimization algorithm.

1 INTRODUCTION

The diameter of a healthy infrarenal abdominal aorta ranges between 15 mm and 24 mm. Abdominal aortic aneurysm (AAA) is diagnosed, if a permanent and irreversible, localized spindle-shaped dilatation of the vessel is found with diameter exceeding 1.5 times the value of the expected normal sate. The rupture of these lesions is extremely hazardous, with fatal outcomes in the overwhelming majority of the cases. Due to modern regular screening tests, the deformations are often noticed at an early stage, and although the elective repair by open surgery or endovascular stent grafting at this point can decrease the mortality ratio significantly, it is still a high risk procedure.

2 MOTIVATION

In clinical practice, the decision on the management of asymptomatic aortic aneurysms is predominantly based upon the maximal diameter of the enlarged lumen and its rate of expansion with critical values being 5.5 cm and 1 cm/year respectively [1]. Although, a strong

correlation has been observed, there is no exact causal relation between these factors and the probability of rupture.

The ineffectiveness of early elective surgical repair [3] and the possible rupture of untreated small aneurysms (dilatations less than 5.5 cm in diameter) [4] raised the demand towards an improved decision strategy founded on mechanical concepts.

From this biomechanical point of view, rupture occurs, when the blood flow induced stress state of the wall reaches beyond the ultimate strength of the tissue. Adopting this concept, patient-specific numerical modelling techniques were applied and reported extensively in the literature.

These methods handle the liquid blood and the solid wall phases separately by solving the respective differential equations in a fully coupled fluid-structure interaction (FSI) algorithm. The displacement field resulting from the finite element modelling (FEM) of the solid phase is the boundary condition for the computer aided fluid dynamics (CFD) simulation of the liquid phase, and conversely, the load field resulting from the CFD simulation is the boundary condition for the FEM. This concept requires an iteration algorithm in each timestep of an unsteady problem until the dynamic equilibrium is fulfilled.

In practice, first, the geometry of the lumen is captured at a single timestep with CTA imaging; the blood pressure is measured usually on the arm, and then transformed to transient volumetric flow rate inlet and the pressure outlet boundary conditions for the examined segment using the method of characteristics on a one-dimensional branching model [5]. With an adequate fluid model for the blood, the CFD calculation yields the pressure acting on the wall, which itself is embedded in a complex, elastic support environment. Finally the FEM, utilizing elaborate material models based on the wall microstructure [6], results in the displacement field, thus closing the iteration step after updating the geometry.

One of the greatest disadvantages of these methods beside the boundary conditions [7] is the lack of individual calibration of the material parameters of the wall.

3 PURPOSE

Our final goal is to introduce a novel method to measure the material parameters in vivo. Thus, not only justifying the eligibility of the wall stresses, but also amending the description of the aneurysm by assessing the state of the material in the degradation process. The procedure involves three cornerstones: the displacement field determination, the corresponding load field calculation and the local identification of the material model parameters, and the assessment of the degree of degradation. The elements of the first one are presented here in details.

4 METHOD

Using ECG-gated CTA images it becomes possible to follow the shape of the arterial wall through a complete cardiac cycle. Then, with a smoothing algorithm, utilizing bicubic spline fitting to the surface in cylindrical coordinates, we can compensate for the measurement errors, assure the continuity of the curvature provide the surface normals in Descartes-coordinates and create the possibility of local mesh refinement. The displacement of each material point is then approximated based on numerical modelling observations. Exploiting periodicity in time, for the velocity and acceleration fields the differentiation of the

displacement field is carried out in the frequency domain after a Fourier transformation. Finally, the strain field and its time derivatives are determined on a surface mesh comprising of 2D simplex first order transverse shear shell elements for further processing. The code and the visualization are developed in Matlab programming environment. We walk through the process examining a real geometry.

4.1 Image acquisition

A Philips Brilliance iCT 256 device was used to scan the abdomen with slice thickness of 1 mm and transversal voxel size of 0.4883 mm. The reconstruction was performed at 10 discrete timesteps of an 833 ms R-R interval with an active contour algorithm resulting in a triangular surface mesh comprising of 23040 elements and 11584 nodes arranged in 181 slices with 2^6 nodes in each cross-section.

4.2 Surface fitting

In need of the surface normals, and since the original mesh did not prove to be readily applicable to strain calculations due to measurement errors and distortions of the elements, from this data we used only the coordinates on the nodes to fit an analytical surface.

The total displacement amplitude of a material point is comparable to the estimated measurement error (identified by the voxel size in the transversal direction), causing an erroneous strain field.

The main axis of the geometry is found by principal component analysis. That is, a straight line is fitted to the nodes by orthogonal distance regression (ODR) given by Eq. 1:

$$\mathbf{r} = \bar{\mathbf{x}} + \mathbf{v} \cdot t, \quad \bar{\mathbf{x}} = \frac{\sum_{i=1}^N \mathbf{x}^i}{N}, \quad \tilde{\mathbf{x}}^i = \mathbf{x}^i - \bar{\mathbf{x}}, \quad \mathbf{X} = \begin{bmatrix} \tilde{x}_1^1 & \tilde{x}_2^1 & \tilde{x}_3^1 \\ \tilde{x}_1^2 & \tilde{x}_2^2 & \tilde{x}_3^2 \\ \vdots & \vdots & \vdots \end{bmatrix}, \quad (1)$$

where $\bar{\mathbf{x}}$ is the mean of the nodal position vectors (\mathbf{x}^i) and \mathbf{v} is the upward pointing eigenvector corresponding to the largest eigenvalue of the $\mathbf{X}^T \mathbf{X}$ matrix, \mathbf{X} being the matrix of the $\bar{\mathbf{x}}$ -centered position vectors ($\tilde{\mathbf{x}}^i$). This line serves as the z axis of the polar coordinate system in which the surface fitting is carried out.

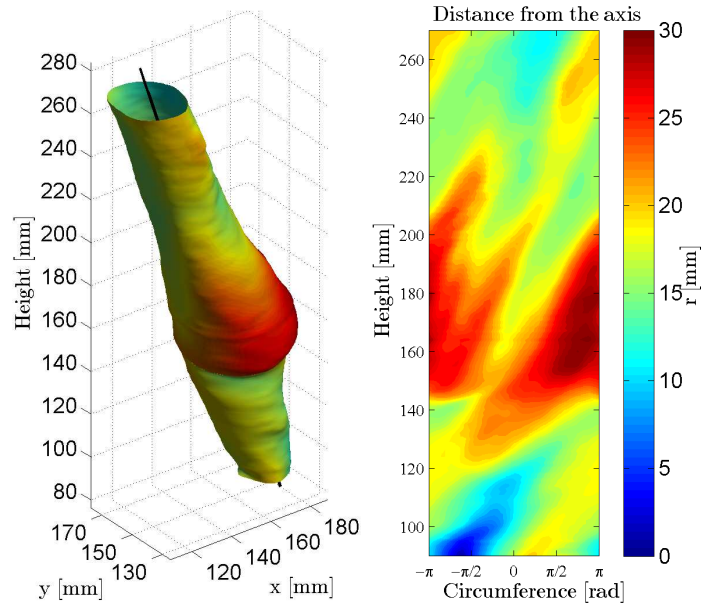


Figure 1: The main axis of the geometry and the surface in polar coordinates. The colour code represents the distance of a point from the axis.

To achieve the C^2 continuity of the surface and avoid the fluctuations of the final strain components, a bicubic spline function was fitted on the nodes. In the circumferential direction a periodic boundary condition was implemented, while for the axial direction the usual boundary condition of prescribing the second directional derivative to be zero was dropped. A parameter study was carried out and concluded, that regarding the deviation of the measured point from the fitted surface in the radial direction, for the patch size – the support domain of the spline basis functions – in the circumferential and axial directions $\pi/20$ and 4 mm respectively prove to be sufficient. As it is shown in Figure 1, with this choice the standard deviation of the sample is 0.0681 mm – with the mean being zero – and only 0.09% of the samples lie outside the interval determined by the transversal voxel size and indicated by red planes in Figure 2 below.

The 2D spline basis functions are defined by Eq. 2 on the $(u, v) \in [0; 1] \times [0; 1]$ interval, outside they are zero.

$$B_{i,j}(u,v) = \frac{N_i(u) \cdot N_j(v)}{36}, \quad \begin{cases} N_1(u) = -u^3 + 3u^2 - 3u + 1 \\ N_2(u) = 3u^3 - 6u^2 + 4 \\ N_3(u) = -3u^3 + 3u^2 + 3u + 1 \\ N_4(u) = u^3 \end{cases}, \quad \begin{matrix} u, v \in [0; 1] \\ i, j = 1 \dots 4 \end{matrix} \quad (2)$$

The spline function value is the linear combination of this 16 basis function (that are not zero on the specific interval) shown in Eq. 3. The derivatives are also linear combinations of the basis function derivatives with the same weights as the original function (see Eq. 4).

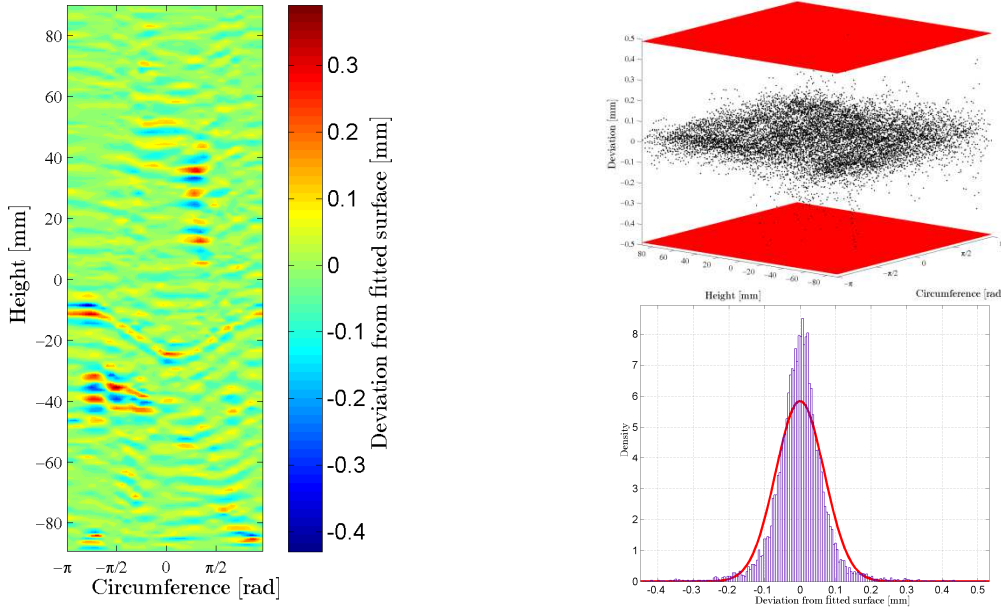


Figure 2: Spatial and statistical distribution of the deviation of the measured point locations from the fitted surface in radial direction. The red surface indicates the estimated confidence of the image acquisition (\pm transversal voxel size).

$$S_{k,l}(u,v) = (\mathbf{uM})\mathbf{W}(\mathbf{M}^T\mathbf{v}^T), \quad \mathbf{u} = \begin{bmatrix} u^3 & u^2 & u & 1 \end{bmatrix}, \quad \mathbf{v} = \begin{bmatrix} v^3 & v^2 & v & 1 \end{bmatrix}, \quad (3)$$

$$\mathbf{M} = \frac{1}{6} \begin{bmatrix} -1 & 3 & -3 & 1 \\ 3 & -6 & 3 & 0 \\ -3 & 0 & 3 & 0 \\ 1 & 4 & 1 & 0 \end{bmatrix}, \quad \mathbf{W} = \begin{bmatrix} w_{11} & w_{12} & w_{13} & w_{14} \\ w_{21} & w_{22} & w_{23} & w_{24} \\ w_{31} & w_{32} & w_{33} & w_{34} \\ w_{41} & w_{42} & w_{43} & w_{44} \end{bmatrix}.$$

$$\frac{\partial S_{k,l}(u,v)}{\partial u} = (\hat{\mathbf{u}}\hat{\mathbf{M}})\mathbf{W}(\mathbf{M}^T\mathbf{v}^T), \quad \hat{\mathbf{u}} = \begin{bmatrix} u^2 & u & 1 \end{bmatrix}, \quad \hat{\mathbf{M}} = \frac{1}{2} \begin{bmatrix} -1 & 3 & -3 & 1 \\ 3 & -6 & 3 & 0 \\ -1 & 0 & 1 & 0 \end{bmatrix}, \quad (4)$$

$$\frac{\partial S_{k,l}(u,v)}{\partial v} = (\mathbf{uM})\mathbf{W}(\hat{\mathbf{M}}^T\hat{\mathbf{v}}^T), \quad \hat{\mathbf{v}} = \begin{bmatrix} v^2 & v & 1 \end{bmatrix}.$$

The smoothing is an ordinary least square (OLS) algorithm minimizing the length of the vector \mathbf{f} containing the difference between the measured (\mathbf{r}) and the estimated surface values at the measured points, where \mathbf{w} is a vector containing the weights of all the basis functions and S_{ij} are the elements of a matrix containing the j^{th} basis function value at the i^{th} node.

$$\mathbf{f}(\mathbf{w}) = \mathbf{S} \cdot \mathbf{w} - \mathbf{r}. \quad (5)$$

4.3 Mesh generation

A structured triangular mesh is generated on the above described surface. Similarly to the input data, the circumference is divided into 64 intervals, and the axial mesh size is kept at 1 mm yielding 21760 elements and 10944 nodes to work with. Note that we cut off 5 mm at

both ends of the model in order for the projection algorithm not to exceed the measured domain.

4.4 Surface normals

The normals of the surface at the new mesh nodes, given by Eq. 6, are visualized in Figure 3. Note, that for better visibility, the shown mesh is 4 times less dense than the one used for the calculations.

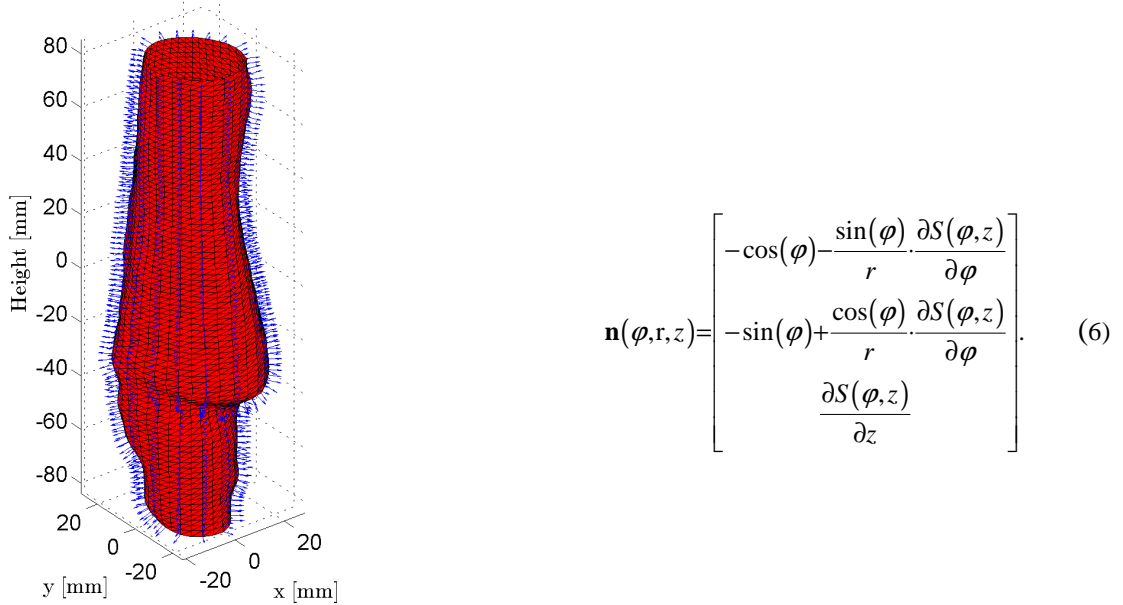


Figure 3: A coarse structured mesh and the normals at the nodes.

4.5 Displacement field

So far we are able to follow the shape of the lumen throughout a stabilized cardiac cycle. To proceed, we need the displacement of the material points as well. To achieve our goal, we have to make certain assumptions on the direction of the movement. After compensating for the rigid body motion by subtracting the displacement of the mass centre from that of the wall, based on FSI simulation observations we assume that each point moves along its normal vector in each time increment. As shown in Figure 4, after the final projection, the point does not find its original position, a closure gap (less than 1% of the displacement amplitude) remains, although the movement is supposed to be periodic in time. We handle this problem by linearly dividing the error among the timesteps.

For the future dynamic analysis the velocity and acceleration fields are also needed. The best approximation, exploiting the periodicity, is the use of a discrete Fourier transform on the displacement vectors and performing the differentiation in the frequency domain through a multiplication.

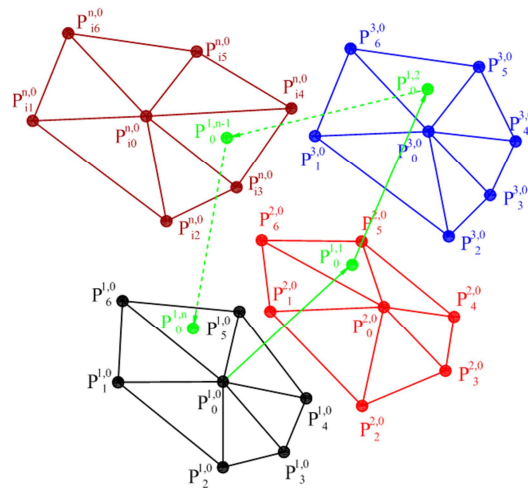


Figure 4: Assumed displacement along the surface normal in each timestep, and the closure gap reaching the initial surface.

Figure 5 shows the displacement amplitude of the surface throughout the cardiac cycle. The values are comparable to the transverse voxel size, thus the smoothing is inevitable. The back part moves with amplitude above 1mm, while the frontal dilated part virtually remains in place, thereby supporting the observation that the dilatation makes the wall less compliant. Similar statements can be made for the velocity and acceleration fields as well.

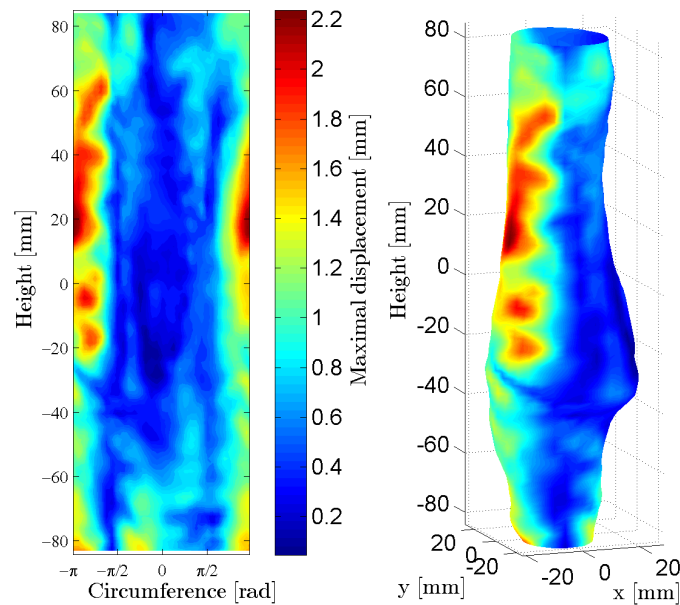


Figure 5: The displacement amplitude of a point in a cardiac cycle. The back part moves with amplitude above 1 mm, while the frontal dilated part virtually remains in place.

4.6 Strain field

Having the nodal displacements at our disposal, the incremental strain field is determined in each timestep by a finite element algorithm. The implemented element type is a laminated, linear simplex Mindlin shell accounting for the shear deformations perpendicular to the reference plane as well. The element local z axis is perpendicular to the reference surface pointing inward the aorta, the x axis is directed upwards and lies in the plane described by the local z and the global axis. The y axis completes the dextral system. The displacements and the strain components are described by the reference surface displacements (indicated by subscript 0) in Eq. 7.

$$\begin{bmatrix} \varepsilon_x \\ \varepsilon_y \\ \gamma_{xy} \\ \gamma_{xz} \\ \gamma_{yz} \end{bmatrix} = \begin{bmatrix} \frac{\partial}{\partial x} & 0 & 0 & 0 & \frac{z \cdot \partial}{\partial x} \\ 0 & \frac{\partial}{\partial y} & 0 & \frac{-z \cdot \partial}{\partial y} & 0 \\ \frac{\partial}{\partial y} & \frac{\partial}{\partial x} & 0 & \frac{-z \cdot \partial}{\partial x} & \frac{z \cdot \partial}{\partial y} \\ 0 & 0 & \frac{\partial}{\partial x} & 0 & 1 \\ 0 & 0 & \frac{\partial}{\partial y} & -1 & 0 \end{bmatrix} \cdot \begin{bmatrix} u_0 \\ v_0 \\ w_0 \\ \varphi_{x0} \\ \varphi_{y0} \end{bmatrix}, \quad (7)$$

$$\begin{aligned} u(x, y, z) &= u_0(x, y) + \varphi_{y0}(x, y) \cdot z, \\ v(x, y, z) &= v_0(x, y) - \varphi_{x0}(x, y) \cdot z, \\ w(x, y, z) &= w_0(x, y). \end{aligned}$$

In Figure 6 and 7 the strain components of the reference plane are shown. It can be concluded that strains in the dilated segment are smaller by an order of magnitude than those of the opposite side. The main constituents there are the circumferential strain and the transversal shear components, each rising up to 20%. The longitudinal strain and the in-plane shear have peaks at locations with high curvature, right under the aneurysm.

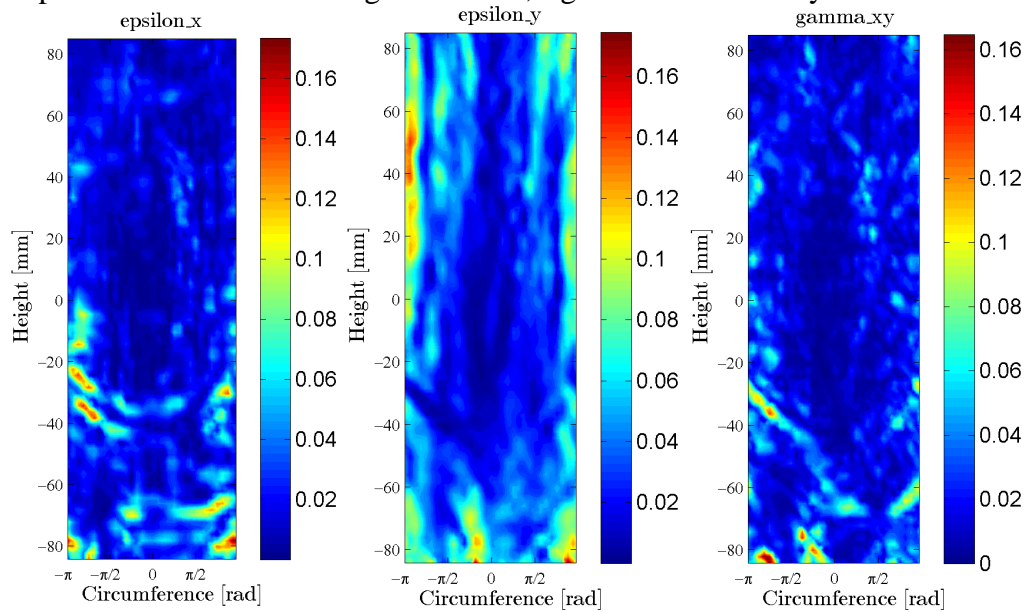


Figure 6: In-plane strain components of the reference surface. From left to right: longitudinal and circumferential strain and in-plane shear.

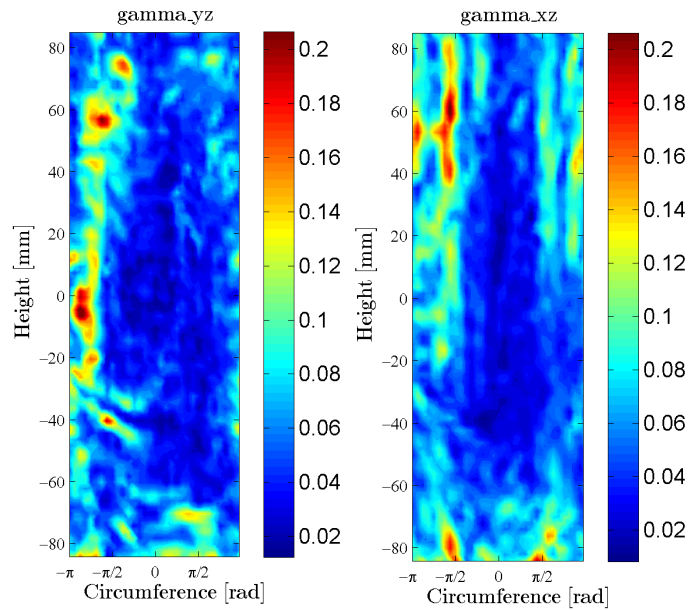


Figure 7: Transversal strain components of the reference surface.

From this point, the next step is to determine a corresponding pressure field resulting from the blood flow. In order to be able to match the phases of the load and displacement fields in the following, we need to determine a common point in both the pressure and the shape measurements. The diastole serves this purpose assuming that the minimal pressure during the cardiac cycle corresponds to the minimal volume enclosed by the deforming surface. We note that depending on the inertia of the wall and the wave effects in it, in some cases, can lead to time delays between them. The occurrence time of the minimal volume is found after fitting a periodic function on the measured data using discrete Fourier transform.

5 CONCLUSIONS

With a quick algorithm developed in Matlab, starting from the segmented images of an aneurysm, we are able to follow the shape of it throughout a cardiac cycle. With a smoothing algorithm we can compensate for the measurement errors. Assuming that the displacements of the material points are normal to the surface and correcting it with the closure error, the displacement field is determined, from which, with the help of a finite element code, the strain components of the aneurysm wall are retrieved and can be analysed and used for further investigations. The strains in the dilated segment are significantly smaller than those of the back side of the aorta (approximately 20%; resulting mainly from the axial strain and the transversal shear constituents), yet the longitudinal strain and the in plane shear are the highest at locations with high curvature, surrounding the bulge region.

REFERENCES

- [1] Hirsch, A. T., Haskal, Z. J., Hertzner, N. R., Bakal, C.W., Creager, M. A., Halperin, J. L., Hiratzka, L. F., Murphy, W. R. C., Olin, J. W., Puschett, J. B., Rosenfield, K. A., Sacks, D., Stanley, J.C., Taylor Jr., L.M., White, C.J., White, J., White, R.A., Antman, E.M., Smith Jr., S.C., Adams, C.D., Anderson, J.L. and Faxon, D.P., Fuster, V., Gibbons, R.J., Halperin, J.L., Hiratzka, L.F., Hunt, S.A., Jacobs, A.K., Nishimura, R., Ornato, J.P., Page, R.L., Riegel, B. *ACC/AHA 2005 Guidelines for the management of patients with peripheral arterial disease (lower extremity, renal, mesenteric, and abdominal aortic)*, Journal of the American College of Cardiology, Vol. 47. (6), pp. 1239-1312. (2006).
- [2] Sakalihasan, N., Limet, R., Defawe, O.D., *Abdominal aortic aneurysm*, The Lancet, 365, pp.1577--89, (2005).
- [3] Powell, J., *Final 12-year follow-up of surgery versus surveillance in the UK small aneurysm trial*, British Journal of Surgery 94 (6), (2007).
- [4] Brewster, D. C., Cronenwett, J. L., Hallett Jr., J. W., Johnston, K. W., Krupski, W. C., Matsumura, J., *Guidelines for the treatment of abdominal aortic aneurysms: Report of a subcommittee of the joint council of the American Association for Vascular Surgery and Society for Vascular Surgery*, Journal of Vascular Surgery 37 (5), pp. 1106-1117., (2003).
- [5] Bárdossy, G., Halász, G., 2011. Modeling blood flow in the arterial system. Periodica Polytechnica 55, 49-55.
- [6] Holzapfel, G.A., Gasser, T.A., Ogden, R.W., *A new constitutive framework for arterial wall mechanics and a comparative study of material models*, J. Elasticity, Vol. 61, pp. 1-48, (2000).
- [7] Józsa, T.I., Paál G., *Boundary conditions for flow simulations of abdominal aortic aneurysms*, International Journal of Heat and Fluid Flow, submitted (Aug. 2013).